Modeling for Control of Very Flexible Aircraft

Travis E. Gibson[*] and Anuradha M. Annaswamy[†]

Massachusetts Institute of Technology, Cambridge, MA, 02139, USA

Eugene Lavretsky[‡]

The Boeing Company, Huntington Beach, CA 92647, USA

Following the NASA Helios flight mishap in 2003 there has been a push for greater understanding of the aerodynamic–structural coupling that occurs in light, very flexible, flying wings.[1] A control oriented model for the longitudinal dynamics of a highly flexible flying wing is developed. Then a comparative analysis of linear and adaptive partial states accessible controllers is presented.

I. Introduction

The first investigations into the dynamics of a highly flexible aircraft came from the Daedalus Project, initiated in 1984.[2,3] The goal of this project was to push the limits of human powered flight while promoting engineering, science and education. Prior to the Daedalus Project the longest distance traveled by a human powered plane was 23 miles, a record set in 1979 with a flight across the English Channel.[4] Over the course of the project the distance record was broken several times and in 1988 *Daedalus 88* flew 73 miles over the Aegean Sea from Iraklion Air Force Base on Crete to Santorini.

Key results from the project were: an attempt to identify stability derivatives for a flexible aircraft using flight data,[5] modeling the aeroelastic characteristics of a highly flexible aircraft,[6] and tools for analyzing aerodynamic and structural loads on flexible–high–aspect–ratio wings under large deformation.[7] Van Schoor et al.[6] identified the importance of including the the flexible states in the stability analysis as the flexible model predicted an unstable phugoid mode with the rigid model predicting a stable phugoid. Building on his work in [7] Drela designed ASWING,[8] a software package used for the study and simulation of flexible aircraft undergoing arbitrarily large deformations.

The Daedalus Project, by design, was a segway to High Altitude Long Endurance (HALE) vehicles. The Helios aircraft, depicted in Figure 1, was developed under the *Environmental Research Aircraft and Sensor Technology* (ERAST) as a HALE class vehicle. The aircraft had two configurations specifically tailored to: 1) high altitude flight and 2) long endurance flight. On August 13th 2001 Helios configuration–1 climbed to a record breaking altitude of 96,863 feet.[1] The second configuration did not have the same success however, and on June 26th 2003 broke apart mid–flight during testing. Throughout the flight the aircraft encountered low–level turbulence. After approximately 30 minutes of flight time a larger than expected wing dihedral formed and the aircraft began a slowly diverging pitch oscillation. The oscillations never subsided and lead to flight speeds beyond the design specifications for Helios. The loading on the aircraft compromised the structure of the aircraft and the skin of the aircraft pulled apart. One of the key recommendations that came from the flight mishap investigation was to, "Develop more advanced, multidisciplinary (structures, aeroelastic, aerodynamics, atmospheric, materials, propulsion, controls, etc) "time-domain" analysis methods appropriate to highly flexible, "morphing" vehicles".[1]

A large body of work on VFA modeling has come since the Helios flight mishap. Patil et al.[9] studied the open loop dynamics of a flying wing structure similar to that of Helios and found that flap positions used to trim the flexible aircraft differ greatly from those used to trim the rigid aircraft. The authors also captured instability in the phugoid mode which is present during large dihedral angles. Similar studies

---

[*]PhD Candidate, Mechanical Engineering, AIAA Student Member, tgibson@mit.edu.
[†]Director AAC Lab, Mechanical Engineering, AIAA Member
[‡]Senior Technical Fellow, Boeing Research and Technology, AIAA Fellow.

American Institute of Aeronautics and Astronautics

Figure 1: NASA Helios in flight.

by Raghavan et al.[10] and Su et al.[11] confirmed this result. In order to validate the modeling approach presented by the authors in [11] the same authors have built an unmanned very flexible UAV called X–HALE with flight tests coming in the future.[12, 13] For a more comprehensive literature review see Ref. [14]. Control designs specifically tailored to flexible aircraft were first proposed by Gregory[15, 16, 17, 18] where output feedback dynamic inversion techniques were modified with a pre–filter to improve the performance of the controller. Dynamic inversion control laws were also presented in [19] and [20] where the robustness of the control designs were tested by introducing uncertainty in the mass of the aircraft.

The authors would like to distinguish between, VFA that can sustain large deviations from trim dihedral (or mode shape) to those aircraft that can not sustain a morphed geometry and simply have structural dynamics on the order of the rigid body dynamics. The term VFA has been used interchangeably for both and so to remove ambiguity from the definition we now refer to the former class as VFA and the latter as simply *Flexible Aircraft* (FA). The former class includes the Helios aircraft and the aircraft geometry of interest for this work. Control designs such as those proposed by Gregory are for FA and not VFA. Implicit in the use of dynamic inversion is the assumption that the stability and control derivatives remain fairly constant. This is not the case with VFA (as was first identified in [9]). Therefore, this work separates itself by addressing the issue of active mode shape control. This idea will be expounded upon later in the paper.

This work looks to address the recommendation from the flight mishap investigation by designing the simplest model of a Very Flexible Aircraft that still captures the unstable phugoid mode. Then, assuming that the dihedral angle, velocity, and pitch rate are the only measurable states, we present control technologies that stabilize the VFA during large dihedral excursions and compare the performance of a linear LQG/LTR controller and an adaptive LQG/LTR controller.[21]

II.   Modeling

II.A.   Vector Notation

Vectors are defined in bold font as

$$\mathbf{U} = U_x\hat{\mathbf{x}} + U_y\hat{\mathbf{y}} + U_z\hat{\mathbf{z}} \tag{1}$$

where $\hat{}$ denotes a unit vector with the triple, $(\hat{\mathbf{x}}, \hat{\mathbf{y}}, \hat{\mathbf{z}})$ orthogonal. The same vector can be defined in two different reference frams using the following notation:

$$\mathbf{U}^{\{1\}} = U_{x_1}\hat{\mathbf{x}}_1 + U_{y_1}\hat{\mathbf{y}}_1 + U_{z_1}\hat{\mathbf{z}}_1 \quad \mathbf{U}^{\{2\}} = U_{x_2}\hat{\mathbf{x}}_2 + U_{y_2}\hat{\mathbf{y}}_2 + U_{z_2}\hat{\mathbf{z}}_2 \tag{2}$$

or in short hand notation,

$$\mathbf{U} = \begin{bmatrix} U_x \\ U_y \\ U_z \end{bmatrix} \tag{3}$$

and similarly

$$\mathbf{U}^{\{1\}} = \begin{bmatrix} U_x \\ U_y \\ U_z \end{bmatrix}^{\{1\}} = \begin{bmatrix} U_{x_1} \\ U_{y_1} \\ U_{z_1} \end{bmatrix} \tag{4}$$

if the specific frame of reference is important.

Tensors are defined in bold font with an over bar as

$$\bar{\mathbf{I}} = \begin{bmatrix} I_{xx} & I_{xy} & I_{xz} \\ I_{yx} & I_{yy} & I_{yz} \\ I_{zx} & I_{zy} & I_{zz} \end{bmatrix} \tag{5}$$

and with the reference frame of the unit vectors included as

$$\bar{\mathbf{I}}^{\{1\}} = \begin{bmatrix} I_{x_1 x_1} & I_{x_1 y_1} & I_{x_1 z_1} \\ I_{y_1 x_1} & I_{y_1 y_1} & I_{y_1 z_1} \\ I_{z_1 x_1} & I_{z_1 y_1} & I_{z_1 z_1} \end{bmatrix} \tag{6}$$

In general a tensor (vector) product is independent of the reference frame, however, if matrix multiplication is to be used then it is necessary that all the tensors (vectors) in the short hand operation are in the same reference frame. When matrix operations are mixed with tensor operations, which will be the case when rotation matrices are used, it is understood the the function operates in the frame of the operand. For instance, let $\mathcal{R}$ be an operator that carries a vector from reference frame 1 to 2, so that

$$\mathbf{U}^{\{2\}} = \mathcal{R} \mathbf{U}^{\{1\}}, \tag{7}$$

see Figure 2a.

II.B.   Linear and Angular Momentum for Generic Bodies

The rate of change of the linear momentum $\boldsymbol{\rho}$ is related to the total external force on the object $\mathbf{F}$ through the following relation

$$\mathbf{F} = \frac{d}{dt} \boldsymbol{\rho}. \tag{8}$$

The angular momentum about an arbitrary point b is defined as $\mathbf{H}_b$ and is related to angular momentum about the center of mass $\mathbf{H}_c$, c denoting the center of mass, and the vector pointing from b to c, $\mathbf{b}_c$ through

$$\mathbf{H}_b = \mathbf{b}_c \times \boldsymbol{\rho} + \mathbf{H}_c, \tag{9}$$

see Figure 2b for an illustration. The time rate of change of the angular momentum about point b is then defined as

$$\mathbf{M}_b = \frac{d}{dt} \mathbf{H}_b \tag{10}$$

where $\mathbf{M}_b$ is the total external moment about b.

Also, note that if the unit vector $\hat{\mathbf{x}}$ is rotating with angular velocity $\boldsymbol{\omega}$, then

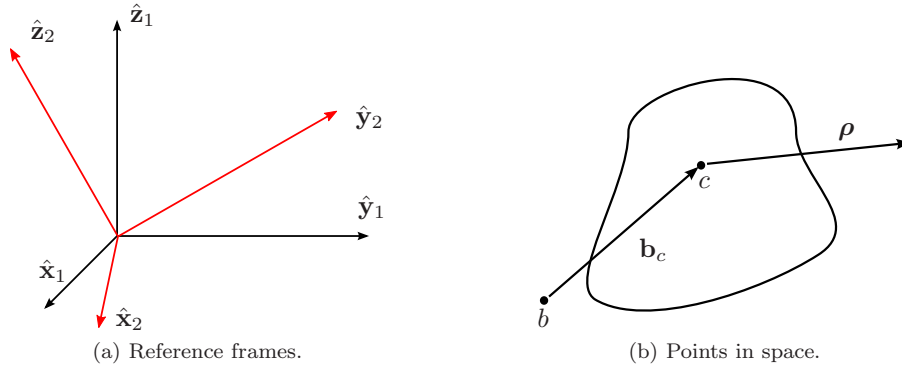$$\frac{d}{dt} \hat{\mathbf{x}} = \boldsymbol{\omega} \times \hat{\mathbf{x}}. \tag{11}$$

(a) Reference frames.   (b) Points in space.

Figure 2: Reference frames and rigid body points of interest.

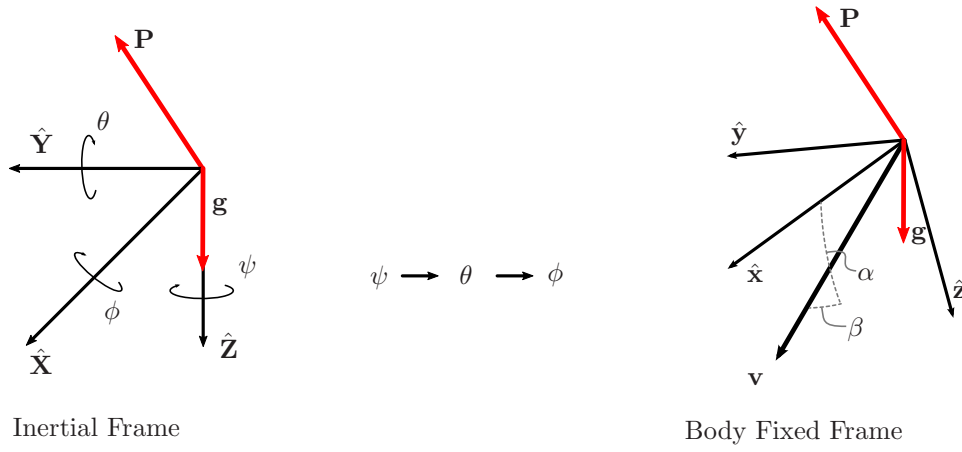American Institute of Aeronautics and Astronautics

Figure 3: Reference frames important for describing aircraft motion.

II.C. Forces and Frames for Aircraft Dynamics

Consider the reference frame relations depicted in Figure 3. Let $(\hat{\mathbf{X}}, \hat{\mathbf{Y}}, \hat{\mathbf{Z}})$ be an inertial frame and let the Euler angles (ϕ, θ, ψ) carry the inertial frame into the body fixed frame $(\hat{\mathbf{x}}, \hat{\mathbf{y}}, \hat{\mathbf{z}})$ via the successive rotations $\psi \to \theta \to \phi$. Letting the aerodynamic force vector from pressure differentials on an aircraft be denoted as $\mathbf{P}$, the transformation from the wind axis forces $\mathcal{L}, \mathcal{C}, \mathcal{D}$, Lift, Drag and Side slip force respectively, to the body fixed frame $(\hat{\mathbf{x}}, \hat{\mathbf{y}}, \hat{\mathbf{z}})$ is realized through

$$\begin{bmatrix} P_x \\ P_y \\ P_z \end{bmatrix} = H_W^B(\alpha, \beta) \begin{bmatrix} -\mathcal{D} \\ -\mathcal{C} \\ -\mathcal{L} \end{bmatrix} \tag{12}$$

with the wind to body axis transformation matrix formally defined as

$$H_W^B(\alpha, \beta) \triangleq \begin{bmatrix} \cos(\alpha)\cos(\beta) & -\cos(\alpha)\sin(\beta) & -\sin(\alpha) \\ \sin(\beta) & \cos(\beta) & 0 \\ \sin(\alpha)\cos(\beta) & -\sin(\alpha)\sin(\beta) & \cos(\alpha) \end{bmatrix} \tag{13}$$

where α is the angle of attack and β is the side slip angle, both of which are defined with respect to the velocity vector $\mathbf{v}$,

$$\begin{aligned} V &= \|\mathbf{v}\| \\ \beta &= \arcsin\left(v_y/V\right) \\ \alpha &= \arctan\left(v_z/v_x\right). \end{aligned} \tag{14}$$

Similarly, the body axis forces can be transformed to the wind axis forces via:

$$H_B^W(\alpha, \beta) \triangleq \left(H_W^B(\alpha, \beta)\right)^{-1}. \tag{15}$$

The gravity vector $\mathbf{g}$ always points in the inertial $\hat{\mathbf{Z}}$ direction, therefore the affect of gravity is realized in the body axis as

$$\mathbf{g} = \begin{bmatrix} g_x \\ g_y \\ g_z \end{bmatrix} = g \begin{bmatrix} -\sin(\theta) \\ \sin(\phi)\cos(\theta) \\ \cos(\phi)\cos(\theta) \end{bmatrix} \tag{16}$$

where g is the gravitational constant.

American Institute of Aeronautics and Astronautics

Figure 4: Artistic rendering of VFA.

II.D. Linear and Angular Momentum for Very Flexible Aircraft

The aircraft of interest is shown in Figure 4. It is comprised of 3 rigid wings with elastic connections adjoining them. Each rigid panel has a propeller for thrust production, an aileron that runs along the aft of the main wing, and an elevator attached at the end of the boom. A schematic of the aircraft with appropriate axes and points of interest labeled is shown in Figure 5.

We are only interested the longitudinal dynamics of this aircraft. Therefore, denoting the angular momentum of the of the center of mass fixed frame (axes–g at point d) as $\boldsymbol{\omega}_d$, it is assumed that

$$\boldsymbol{\omega}_d^{\{g\}} = \begin{bmatrix} 0 \\ \omega_{d,y_g} \\ 0 \end{bmatrix} \tag{17}$$

and the velocity of the center of mass in frame–g is assumed to be of the form:

$$\mathbf{v}_d^{\{g\}} = \begin{bmatrix} v_{d,x_g} \\ 0 \\ v_{d,z_g} \end{bmatrix}. \tag{18}$$

Letting $\mathbf{F}$ be the total force acting on the system of 3 wings, the linear momentum of the system changes as:

$$
\begin{aligned}
\mathbf{F} &= \frac{d}{dt}\boldsymbol{\rho}_d \\
&= m\left(\dot{v}_{d,x_g}\hat{\mathbf{x}}_g + \dot{v}_{d,z_g}\hat{\mathbf{z}}_g\right) + m\left(v_{d,x_g}\omega_{d,y_g}(\hat{\mathbf{y}}_g \times \hat{\mathbf{x}}_g) + v_{d,z_g}\omega_{d,y_g}(\hat{\mathbf{y}}_g \times \hat{\mathbf{z}}_g)\right) \\
&= m\left(\left(\dot{v}_{d,x_g} + v_{d,z_g}\omega_{d,y_g}\right)\hat{\mathbf{x}}_g + \left(\dot{v}_{d,z_g} - v_{d,x_g}\omega_{d,y_g}\right)\hat{\mathbf{z}}_g\right)
\end{aligned}
\tag{19}
$$

where m is the total mass of the system given as $m = 3m^*$ with m^* denoting the mass of one of the three identical panels making up the flying wing.

The total Moment acting on the system of three wings about point d is defined as $\mathbf{M}$ and the time rate of change of the angular momentum about d is governed by

$$
\begin{aligned}
\mathbf{M} &= \frac{d}{dt}\mathbf{H}_d \\
&= \frac{d}{dt}\bar{\mathbf{I}}_d\boldsymbol{\omega}_d + \bar{\mathbf{I}}_d\frac{d}{dt}\boldsymbol{\omega}_d
\end{aligned}
\tag{20}
$$

Figure 5: Schematic of VFA.

American Institute of Aeronautics and Astronautics
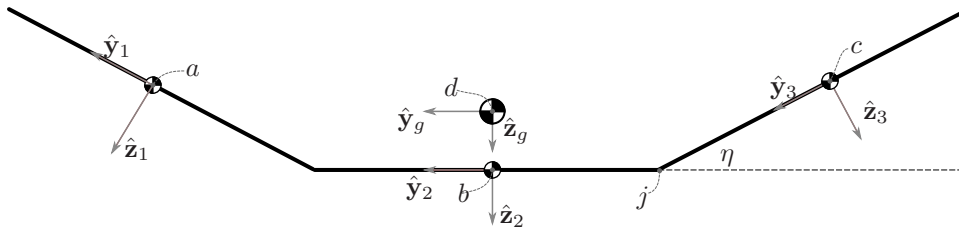
where $\bar{\mathbf{I}}_d$ is the moment of inertia for the entire wing about the center of mass at point d. Time rate of change of angular velocity reduces as

$$\frac{d}{dt}\boldsymbol{\omega}_d = \dot{\omega}_{d,y_g}\hat{\mathbf{y}}_g + \omega_{d,y_g}\left(\omega_{d,y_g}\hat{\mathbf{y}}_g \times \hat{\mathbf{y}}_g\right)$$
$$= \dot{\omega}_{d,y_g}\hat{\mathbf{y}}_g. \tag{21}$$

Next we investigate the moment of inertia. The total moment of inertia has been defined as $\bar{\mathbf{I}}$. Now let the moment of inertia for each individual wing about its respective center of mass be defined as $\bar{\mathbf{I}}^*$. The moment of inertia then for the the wing in frame–3 about point d is then:

$$\bar{\mathbf{I}}^*_{d,\text{wing}-3} = \bar{\mathbf{I}}^* + m^*\left(\langle \mathbf{c}_d, \mathbf{c}_d\rangle I - \mathbf{c}_d \otimes \mathbf{c}_d\right) \tag{22}$$

where $\mathbf{c}_d$ is the vector from point c to point d, $\langle \cdot, \cdot \rangle$ is the inner product operator, I is a 3×3 identity matrix carrying the inner product into the tensor space and $\otimes$ is the outer product. The moment of inertia for wings 1 and 2 can be calculated and hence forth denoted as $\bar{\mathbf{I}}^*_{d,\text{wing}-1}$ and $\bar{\mathbf{I}}^*_{d,\text{wing}-2}$. Then the total moment of inertia for the entire system becomes

$$\bar{\mathbf{I}} = \bar{\mathbf{I}}^*_{d,\text{wing}-1} + \bar{\mathbf{I}}^*_{d,\text{wing}-2} + \bar{\mathbf{I}}^*_{d,\text{wing}-3}. \tag{23}$$

Given that the angular velocity only has a non–zero component in the y_g axis, the only component from the moment of inertia that is important is $I_{y_g y_g}$ where

$$I_{y_g y_g} = c_1 + c_2 \sin^2(\eta) \tag{24}$$

with

$$c_1 = 3I^*_{yy}$$
$$c_2 = 2I^*_{zz} - 2I^*_{yy} + m^*\frac{s^2}{6}. \tag{25}$$

The only unknown quantity is the time varying nature of the dihedral angle. Up until this point the equations of motion have all been calculated from the center of mass of the entire system. In what follows we derive the dynamics of the dihedral angle from point j.

$$\mathbf{H}^*_j = \mathbf{j}_c \times \boldsymbol{\rho}^* + \mathbf{H}^*_c$$
$$= -\frac{s}{2}\hat{\mathbf{y}}_3 \times m^*\begin{bmatrix} v_{c,x3} \\ v_{c,y3} \\ v_{c,z3} \end{bmatrix} + \begin{bmatrix} I^*_{x_3 x_3} & 0 & 0 \\ 0 & I^*_{y_3 y_3} & 0 \\ 0 & 0 & I^*_{z_3 z_3} \end{bmatrix}\begin{bmatrix} \omega_{c,x3} \\ \omega_{c,y3} \\ \omega_{c,z3} \end{bmatrix} \tag{26}$$

where the angular momentum of frame–3, denoted as $\boldsymbol{\omega}_c$ is related to the angular momentum in frame–2, $\boldsymbol{\omega}_b = \boldsymbol{\omega}_d$ by the following:

$$\begin{bmatrix} \omega_{c,x3} \\ \omega_{c,y3} \\ \omega_{c,z3} \end{bmatrix} = \begin{bmatrix} 1 & 0 & 0 \\ 0 & \cos\eta & \sin\eta \\ 0 & -\sin(\eta) & \cos(\eta) \end{bmatrix}\begin{bmatrix} \omega_{d,x2} \\ \omega_{d,y2} \\ \omega_{d,z2} \end{bmatrix} + \begin{bmatrix} \dot{\eta} \\ 0 \\ 0 \end{bmatrix} \tag{27}$$

and noting that $\omega_{d,x3} = \omega_{d,z3} = 0$, the angular momentum of frame–3 about point j becomes

$$\mathbf{H}^*_j = \begin{bmatrix} -\frac{s}{2}m^* v_{c,z3} \\ 0 \\ \frac{s}{2}m^* v_{c,x3} \end{bmatrix} + \begin{bmatrix} I^*_{x_3 x_3}\dot{\eta} \\ I^*_{y_3 y_3}\cos(\eta)\omega_{d,y2} \\ -I^*_{z_3 z_3}\sin(\eta)\omega_{d,y2} \end{bmatrix}. \tag{28}$$

The angular momentum $\mathbf{H}^*_j$ is then expanded so that all of the velocity components are with respect to

American Institute of Aeronautics and Astronautics

frame–2 (see Appendix B.1)

$$
\mathbf{H}_j^* = \underbrace{\left(-\tfrac{s}{2}m^*\left(\left(v_{d,z_2} + \frac{s}{3}\cos(\eta)\dot\eta\right)\cos(\eta) - \dot\eta\frac{s}{2}\right) + I^*_{x_3 x_3}\dot\eta\right)\hat{\mathbf{x}}_3}_{\mathbf{h_1}}
$$
$$
+ \underbrace{\left(I^*_{y_3 y_3}\cos(\eta)\omega_{d,y_2}\right)\hat{\mathbf{y}}_3}_{\mathbf{h_2}}
$$
$$
+ \underbrace{\left(\tfrac{s}{2}m^*\left(v_{d,x_2} - \frac{s}{6}\sin(\eta)\omega_{d,y_2}\right) - I^*_{z_3 z_3}\sin(\eta)\omega_{d,y2}\right)\hat{\mathbf{z}}_3}_{\mathbf{h_3}}
$$

(29)

Taking the time derivative $\mathbf{H}_j^*$ (See Appendix B.2), the x–axis moment relation becomes

$$
M^*_{j,x_3} - \kappa_c\dot\eta - \kappa_k\eta = -\tfrac{s}{2}m^*\left(\dot v_{d,z_2}\cos(\eta) - v_{d,z_2}\sin(\eta)\dot\eta - \frac{s}{3}\cos^2(\eta)\ddot\eta + 2\frac{s}{3}\cos(\eta)\sin(\eta)\dot\eta^2\right)
$$
$$
+ \left(I^*_{x_3 x_3} + m^*\tfrac{s^2}{4}\right)\ddot\eta + \left(I^*_{y_3 y_3}\cos(\eta)\omega_{d,y_2}\right)\sin(\eta)\omega_{d,y_2}
$$
$$
\left(\tfrac{s}{2}m^*\left(v_{d,x_2} - \frac{s}{6}\sin(\eta)\omega_{d,y_2}\right) - I^*_{z_3 z_3}\sin(\eta)\omega_{d,y2}\right)\cos(\eta)\omega_{d,y_2}.
$$

(30)

where M^*_{j,x_3} is the total external moment acting on joint–j through wing–3, κ_c is the damping coefficient for the joint and κ_k is the spring constant for the joint.

II.E. Forces and Moments acting on VFA in Stability Axis Frame

The loads on an airfoil are defined in the wind axis frame. Using the relations illustrated in Figure 3, we denote the magnitude of the velocity at the center of mass as V and the angle of attack as α, note that $\beta = 0$. The three panels each have their own local (V_i, α_i, β_i) $i = 1, 2, 3$, see Appendix B.3 for more details. For ease of exposition and to conform with historical notation the pitch rate of the center of mass frame is redefined as $q \triangleq \omega_{d,y_g}$.

The total wind axis forces defined with respect to the center of mass of the vehicle are denoted

$$
\mathbf{W} = \begin{bmatrix} -\mathcal{D} \\ 0 \\ -\mathcal{L} \end{bmatrix}
$$

(31)

which are defined relative to the body axis forces through the center of gravity body fixed frame g as:

$$
\mathbf{W} = H_B^W(\alpha, \beta)\left(\mathbf{P}_w^{\{g\}} + \mathbf{P}_t^{\{g\}}\right)
$$

(32)

where $\mathbf{P}_w$ is the resultant pressure driven force from the three wing sections

$$
\mathbf{P}_w^{\{g\}} = \underbrace{R_x(\eta)H_W^B(\alpha_1, \beta_1)\mathbf{W}_{w,1}^*}_{\mathbf{P}_{w,1}^*} + \underbrace{H_W^B(\alpha_2, \beta_2)\mathbf{W}_{w,2}^*}_{\mathbf{P}_{w,2}^*} + \underbrace{R_x(-\eta)H_W^B(\alpha_3, \beta_3)\mathbf{W}_{w,3}^*}_{\mathbf{P}_{w,3}^*}
$$

(33)

and where $\mathbf{P}_t$ is the resultant pressure driven force from the three tail sections

$$
\mathbf{P}_t^{\{g\}} = \underbrace{R_x(\eta)H_W^B(\alpha_1, \beta_1)\mathbf{W}_{t,1}^*}_{\mathbf{P}_{t,1}^*} + \underbrace{H_W^B(\alpha_2, \beta_2)\mathbf{W}_{t,2}^*}_{\mathbf{P}_{t,2}^*} + \underbrace{R_x(-\eta)H_W^B(\alpha_3, \beta_3)\mathbf{W}_{t,3}^*}_{\mathbf{P}_{t,3}^*}.
$$

(34)

Both of which are part of the total force acting on the body:

$$
\mathbf{F}^{\{g\}} = \mathbf{P}_w^{\{g\}} + \mathbf{P}_t^{\{g\}} + \mathbf{T}^{\{g\}} + \mathbf{g}^{\{g\}}.
$$

(35)

The local pressure driven forces defined in the local stability axes are given by

$$
\mathbf{W}_{w,i}^* = \begin{bmatrix} -\mathcal{D}_{w,i}^* \\ 0 \\ -\mathcal{L}_{w,i}^* \end{bmatrix} \qquad \mathbf{W}_{t,i}^* = \begin{bmatrix} -\mathcal{D}_{t,i}^* \\ 0 \\ -\mathcal{L}_{t,i}^* \end{bmatrix} \qquad i = 1, 2, 3
$$

(36)

American Institute of Aeronautics and Astronautics

and the total thrust as

$$\mathbf{T} = \begin{bmatrix} \mathcal{T} \\ 0 \\ 0 \end{bmatrix} = \sum_{i=1}^{3} \underbrace{\begin{bmatrix} \mathcal{T}_i^* \\ 0 \\ 0 \end{bmatrix}}_{\mathbf{T}_i^*} \tag{37}$$

where T_i^* are the thrust force vectors applied on each wing by a propeller engine. The local lift and drag on the wing and tail sections are defined as:

$$\mathcal{L}_{w,i}^* = \bar{\rho}_i^* C_{\mathcal{L}_{w,i}} S_w^* \qquad\qquad C_{\mathcal{L}_{w,i}} = C_{\mathcal{L}_\alpha} \alpha_i + C_{\mathcal{L}_\delta} \delta_{a,i} \tag{38}$$

$$\mathcal{L}_{t,i}^* = \bar{\rho}_i^* C_{\mathcal{L}_{t,i}} S_t^* \qquad\qquad C_{\mathcal{L}_{t,i}} = C_{\mathcal{L}_\alpha} (\alpha_i + \delta_{e,i}) \tag{39}$$

$$\mathcal{D}_{w,i}^* = \bar{\rho}_i^* C_{\mathcal{D}_{w,i}} S_w^* \qquad\qquad C_{\mathcal{D}_{w,i}} = C_{D0} + \kappa_{\mathcal{D}} C_{\mathcal{L}_{w,i}}^2 \tag{40}$$

$$\mathcal{D}_{t,i}^* = \bar{\rho}_i^* C_{\mathcal{D}_{t,i}} S_t^* \qquad\qquad C_{\mathcal{D}_{t,i}} = C_{D0} + \kappa_{\mathcal{D}} C_{\mathcal{L}_{t,i}}^2 \tag{41}$$

where $\bar{\rho}_i^*$ is the local dynamic pressure at the center of each wing, S_w^* is the area of the wing and S_t^* is the area of the tail, $\delta_{a,i}$ are the aileron deflection angles and $\delta_{e,i}$ are the elevator deflection angles with $i = 1, 2, 3$.

The total moment on the aircraft is parameterized as

$$\begin{bmatrix} 0 \\ \mathcal{M} \\ 0 \end{bmatrix} = \mathbf{M}^{\{g\}} = \sum_{i=1}^{3} \left(\mathbf{M}_i^* + \mathbf{l}_{w,i} \times \mathbf{P}_{w,i}^* + \mathbf{l}_{t,i} \times \mathbf{P}_{t,i}^* \right), \quad M_i^* = \begin{bmatrix} 0 \\ \mathcal{M}_i^* \\ 0 \end{bmatrix} \tag{42}$$

and

$$\mathcal{M}_i^* = \bar{\rho}_i^* C_{\mathcal{M}_i} c_w S_w^* \qquad C_{\mathcal{M}_i} = C_{\mathcal{M}_0} + C_{\mathcal{M}_\delta} \delta_{a,i} \tag{43}$$

where c_w is the cord length of the wing, and $\mathbf{l}_{w,i}$ and $\mathbf{l}_{t,i}$ are the vectors that point from the quarter cord of the wing to the center of mass and the vectors that point from the quarter chord of the tail to center of mass, respectively. The length of the boom connecting from the quarter cord of the wing to the quarter cord of the tail is denoted l_b. Finally, the hinge moment at j acting on wing–3 in the x–direction is redefined as

$$\mathcal{H} \triangleq M_{j,x_3}^* = -(P_{w,1_z}^* + P_{t,1_z}^*) - m^* g \cos(\eta) \cos(\theta) \tag{44}$$

The dynamics for the VFA can now be be compactly expressed in the wind axis as:

$$\begin{aligned}
\dot{V} &= (\mathcal{T} \cos\alpha - \mathcal{D})/m - g \sin\gamma \\
\dot{\alpha} &= -(\mathcal{T} \sin\alpha + \mathcal{L})/(mV) + q + g \cos(\gamma/V) \\
\dot{h} &= V \sin\gamma \\
\dot{\theta} &= q \\
\dot{q} &= \frac{\mathcal{M} - 2c_2 \sin(\eta) \cos(\eta) \dot{\eta} q}{c_1 + c_2 \sin^2(\eta)} \\
\ddot{\eta} &= \frac{\mathcal{H} - \kappa_c \dot{\eta} - \kappa_k \eta + d_1 - d_2}{d_3}
\end{aligned} \tag{45}$$

where h is the height, $\gamma = \theta - \alpha$, and

$$\begin{aligned}
c_1 &= 3I_{yy}^* \\
c_2 &= 2I_{zz}^* - 2I_{yy}^* + m^* \frac{s^2}{6} \\
d_1 &= \frac{s}{2} m^* \left(\left(\dot{V} \sin(\alpha) + V \cos(\alpha)\dot{\alpha} \right) \cos(\eta) - V \sin(\alpha) \sin(\eta)\dot{\eta} - 2\frac{s}{3} \cos(\eta) \sin(\eta)\dot{\eta}^2 \right) \\
d_2 &= \left(I_{yy}^* - I_{zz}^* - m^* \frac{s^2}{12} \right) \sin(\eta) \cos(\eta) q^2 - \frac{s}{2} m^* \cos(\eta) V \cos(\alpha) q \\
d_3 &= I_{x_3 x_3}^* + m^* \left(\frac{s^2}{4} + \frac{s^2}{6} \cos^2(\eta) \right).
\end{aligned} \tag{46}$$

The geometric parameters and aerodynamic coefficients for the VFA are listed in Table 1.

III. Trim Analysis

A trim analysis is now carried out to ensure that the VFA model presented captures the unstable phugoid mode that was observed in the higher fidelity models.[9, 10, 11] The nonlinear dynamics in (45) can be compactly expressed as

$$\dot{X} = f(X, U) \tag{47}$$

where X is the state vector and U is the control input:

$$
\begin{aligned}
X &= \begin{bmatrix} V & \alpha & h & \theta & q & \eta & \dot{\eta} \end{bmatrix}^T \\
U &= \begin{bmatrix} \delta_{a_c} & \delta_{a_o} & \delta_{e_c} & \delta_{e_o} & \delta_{\mathcal{T}} \end{bmatrix}^T.
\end{aligned}
\tag{48}
$$

The subscript a_c and a_o signify aileron center and aileron outer respectively so that $\delta_{a_c} = \delta_{a_2}$ and $\delta_{a_o} = \delta_{a_i}$ where i=1,3. The subscripts e_c and e_o signify elevator center and elevator outer respectively. The control input $\delta_{\mathcal{T}} = \mathcal{T}_i$, $i = 1, 2, 3$. The linear dynamics are then defined as:

$$\dot{x} = Ax + Bu + \epsilon(X, U) \tag{49}$$

where $x = X - X_0$, $u = U - U_0$ with X_0 the trim state and U_0 the trim input satisfying $0 = f(X_0, U_0)$,

$$
A = \left. \frac{\partial f(X, U)}{\partial X} \right|_{\substack{X = X_0 \\ U = U_0}} \qquad B = \left. \frac{\partial f(X, U)}{\partial U} \right|_{\substack{X = X_0 \\ U = U_0}}
\tag{50}
$$

and ϵ is the linearization error.

The nonlinear VFA dynamics in (47) were linearized at a velocity of 30 ft/s and a height of 40,000 ft with the dihedral angle varied from 0 to 45 degrees. The trim states and trim inputs are shown in Figure 6. As the dihedral angle is increased the angle of attack also increases. This is to be expected, as the the dihedral angle is increased the local angles of attack at the outer wings is reduced and their lift contributions reduce as well. Therefore the angle of attack with respect to the center airfoil must increase to compensate for the reduced lift from the outer wings. Given that the aircraft has multiple control surfaces (aileron and elevator for each wing section) there is a degree of redundancy, which is what allows the aircraft to be trimmed at any desired dihedral angle.
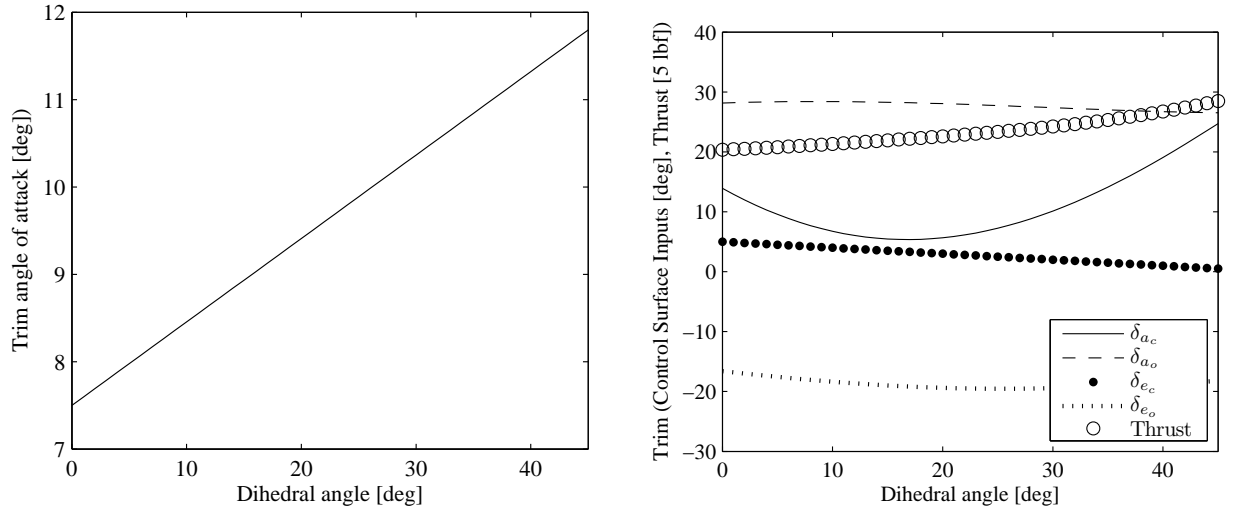
(a) As the dihedral angle increases the baseline angle of attack must increase in order to compensate for the loss of lift from the outer wings, where the local lift is inversely proportional to dihedral.

(b) There is a degree of redundancy in the control surfaces (each wing section has an aileron and an elevator. This is what allows the VFA to be trimmed at arbitrary dihedral for a given airspeed.)

Figure 6: Trim results.

American Institute of Aeronautics and Astronautics

The eigen values from the same study are shown in Figure 7. At zero dihedral angle the short period mode is lightly damped and the phugoid mode is stable. As the dihedral angle increases the pitch moment of inertia increases, leading to increased damping in the short period mode and instability in the phugoid mode. The transition to instability occurs at a dihedral angle of 15 degrees. These results agree with the findings from Ref. 9.

For the next study the aircraft was trimmed at a dihedral angle of 5 degrees. The trim inputs were held fixed while the dihedral angle initial condition was varied from 10 to 20 degrees in 5 degree increments so as to observe the open–loop behavior of the aircraft. These results are shown in Figure 8. For initial conditions of 10 and 15 degrees in dihedral angle the aircraft exhibits steady motion as the dihedral slowly approaches the trim condition. For large perturbation from trim the dihedral angle quickly diverges. This illustrates that the VFA linearizion results are only valid for small perturbations from dihedral trim and thus active dihedral control is necessary.

(a) Zoom out of all eigen values.

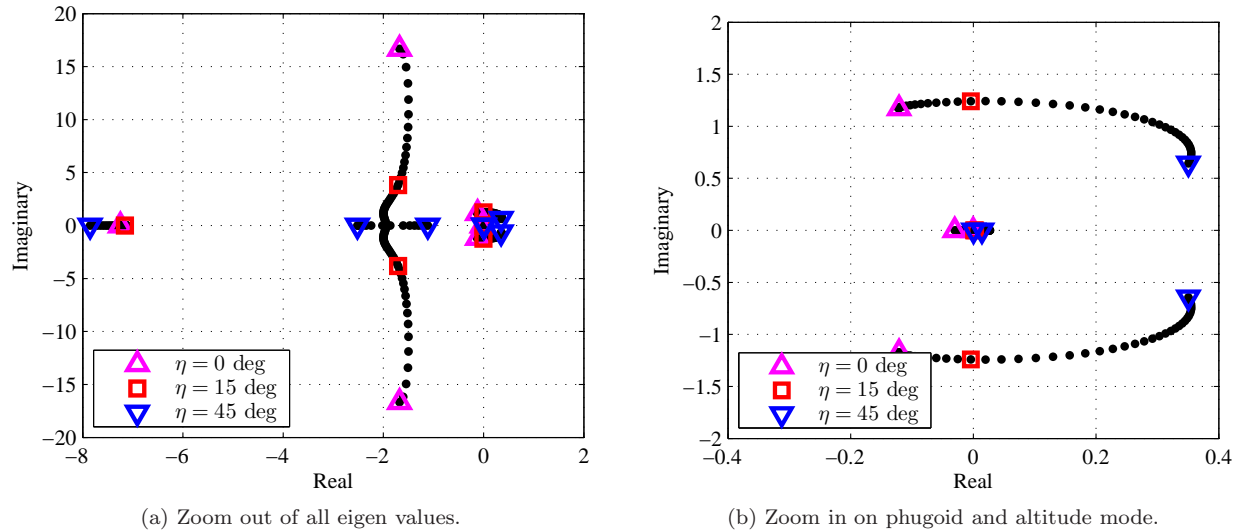(b) Zoom in on phugoid and altitude mode.

Figure 7: Eigen values for trim points. At zero dihedral angle the short period mode is lightly damped and the phugoid mode is stable. As the dihedral angle increases the short period mode damping increases and the phugoid mode becomes unstable.
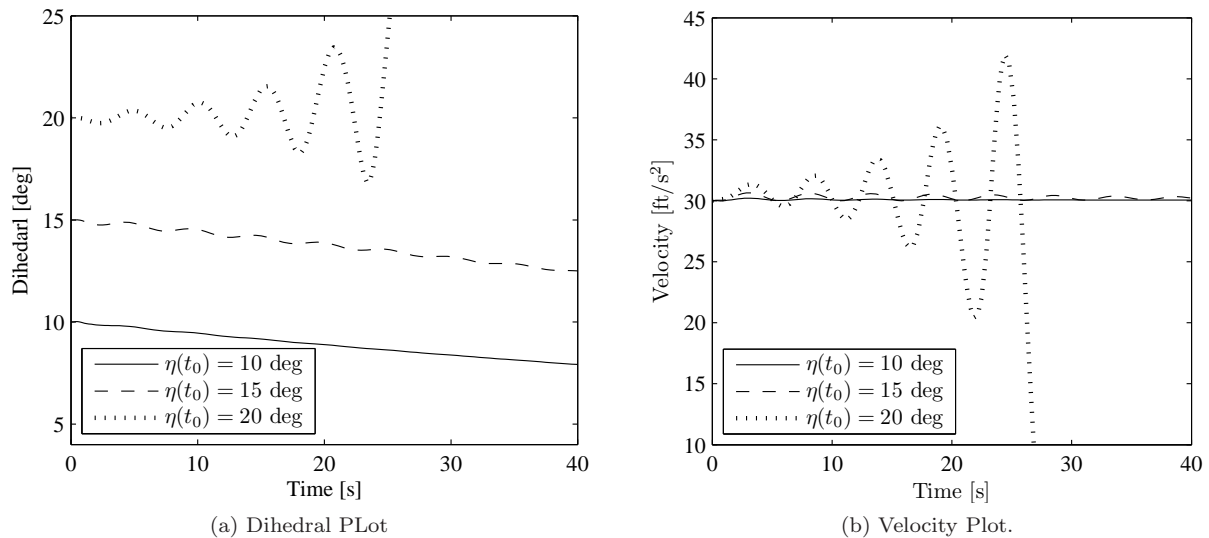

(a) Dihedral PLot

(b) Velocity Plot.

Figure 8: Initial condition perturbation from trim input for dihedral angle of 5 degrees.

American Institute of Aeronautics and Astronautics

IV. Control Design

In flight disturbances, such as wind gusts, will cause the dihedral angle to deviate from trim. Given that the phugoid mode can become unstable when the dihedral angle is increased, actively controlling the wing shape is a necessity. For most aircraft, sensors are not deployed to measure mode shape. In fact, when control methodologies were first proposed for highly flexible aircraft it was assumed that the mode shape was not measurable.[15] Gregory's dynamic inversion architecture was only for control of *Flexible Aircraft*, thus it was not necessary for the dihedral angle to be measured. In the case of *Very Flexible Aircraft* the dynamic inversion controller as proposed in [18] is no longer appropriate as the structure of the Input Jacobian, B, can change (i.e. with varying dihedral, ailerons and elevators loose control surface effectiveness in some axes while gaining control surface effectiveness in others). While the linearized dynamics in (49) are valid, notice that during large dihedral excursions from trim ϵ will grow large. An equivalent representation for the nonlinear dynamics is that of a *Linear Parameter Varying* (LPV) system of the form:

$$\dot{x} = \bar{A}(V,h,\eta)x + \bar{B}(V,h,\eta) + \bar{\epsilon}(X,U) \tag{51}$$

where the Linear Time Invariant (LTI) matrices from (49) have been replaced by matrices that vary in the parameter space (V,h,η) and $\bar{\epsilon}$ arbitrarily small, even for large trim deviations. For rigid aircraft it is common to gain schedule a controller with respect to the height and velocity of the aircraft, essentially compensating for the affect of dynamic pressure change. In this case, the dihedral change is also critical and in addition its affects on loading not completely known. Also, note that when the states and inputs are at trim value,

$$\bar{A}(V_0,h_0,\eta_0) = A \text{ and } \bar{B}(V_0,h_0,\eta_0) = B, \tag{52}$$

where the subscript 0 denotes trim value.

The control problem is outlined as follows. The inputs available for control are the Thrust $\mathcal{T}$, center elevator δ_{e_c} and the outer ailerons δ_{a_o}, the other inputs, δ_{e_c} and δ_{o_c} are fixed at trim. The available outputs are the Velocity V, the dihedral angle η, and the pitch rate q. At trim, (49), the measurable states are related to the entire state vector by

$$y = Cx \tag{53}$$

where y is the measured output $[\Delta V \ \Delta q \ \Delta \eta]^T$, and $u = [\Delta \mathcal{T} \ \Delta\delta_{e_c} \ \Delta\delta_{a_o}]^T$ where the Δ signifies deviations from trim. The goal is to design u such that the control input $U = U_0 + u$ returns the system of equations back to trim in the presence of initial condition perturbations in dihedral angle. Given that only a subset of the state space is measurable an optimal high gain observer will be used to rebuild an estimate of the state space. The baseline controller then uses feedback from the full state of the observer dynamics, $\hat{x}$. The adaptive controller augments the baseline controller with observer feedback through time varying gain, $\theta(t)$. In order for the control laws discussed below to be implemented the following assumptions must hold:

- (A,B) is controllable and (A,C) is observable.

- $\det (CB) \neq 0$.

- $C(sI - A)^{-1}B$ is minimum phase.

The state estimate $\hat{x}$ is generated through

$$\dot{\hat{x}} = (A - LC)\hat{x} + Bu + Ly \tag{54}$$

where

$$L = P_o C^T R_o^{-1} \tag{55}$$

with $P_o = P_o^T > 0$ the solution to the *Observer Algebraic Riccati Equation* (OARE)

$$P_o(A + \lambda I)^T + (A + \lambda I)P_o - P_o C^T R_o^{-1} C P_o + Q_o = 0. \tag{56}$$

The weighting parameters (Q_o, R_o), both symmetric and positive definite are defined as

$$Q_o = Q_0 + \frac{\nu^2 + 1}{\nu^2}BB^T, \quad R_o = \frac{\nu^2}{\nu^2 + 1}R_0 \tag{57}$$

American Institute of Aeronautics and Astronautics

where Q_0 and R_0 are symmetric positive definite free design parameters, ν is a small gain parameter and λ guaranteeing that all the Eigen Values of $A - LC$ are less than $-\lambda$.

The control input for the baseline controller is then defined as $u = -K\hat{x}$,

$$K = P_c B R_c^{-1} \tag{58}$$

with $P_c = P_c^T > 0$ the solution to the *Control Algebraic Riccati Equation* (CARE)

$$P_c A + A^T P_c - P_c B R_c^{-1} B^T P_c + Q_c = 0. \tag{59}$$

The free design weights (Q_c, R_c), are both symmetric and positive definite. The baseline control input can be compactly expressed as:

$$u = -K\hat{x}, \quad \dot{\hat{x}} = (A - LC - BK)\hat{x} + Ly, \tag{60}$$

where the free design parameters for the observer and linear control design are $(\lambda, \nu, Q_0, R_0, Q_c, R_c)$.

The adaptive control augments the baseline control input so that

$$u = -K\hat{x} + \theta^T(t)\hat{x} \tag{61}$$

where the adaptive gain θ is time varying, K is the same fixed gain as defined in (58) and $\hat{x}$ is the same as that defined in (60). The adaptive gain is adjusted as

$$\dot{\theta} = \mathrm{Proj}\left(\theta, -\Gamma \hat{x} e_y^T R_0^{-1} W, F(\theta; \vartheta, \varepsilon)\right) \tag{62}$$

where

$$\begin{aligned} e_y &= y - \hat{y} \\ W &= VU^T \\ B^T C^T R_0^{-\frac{1}{2}} &= U\Lambda V^T, \end{aligned} \tag{63}$$

F is a collection of convex functions as defined in (79) with ε and ϑ scalars that describe the upper bound on the adaptive parameter and Γ controls the rate of adaptation. In addition to the observer and baseline control free design parameters, the adaptive controller is uniquely defined by the choice of $(\Gamma, \vartheta, \varepsilon)$.

Note that the adaptive input does not feed directly into the observer with the observer dynamics evolving the same as before, $\dot{\hat{x}} = (A - LC - BK)\hat{x} + Ly$. For a detailed presentation and analysis of the adaptive controller see [21]. Schematic representations for the two controllers can be found in Figure 9
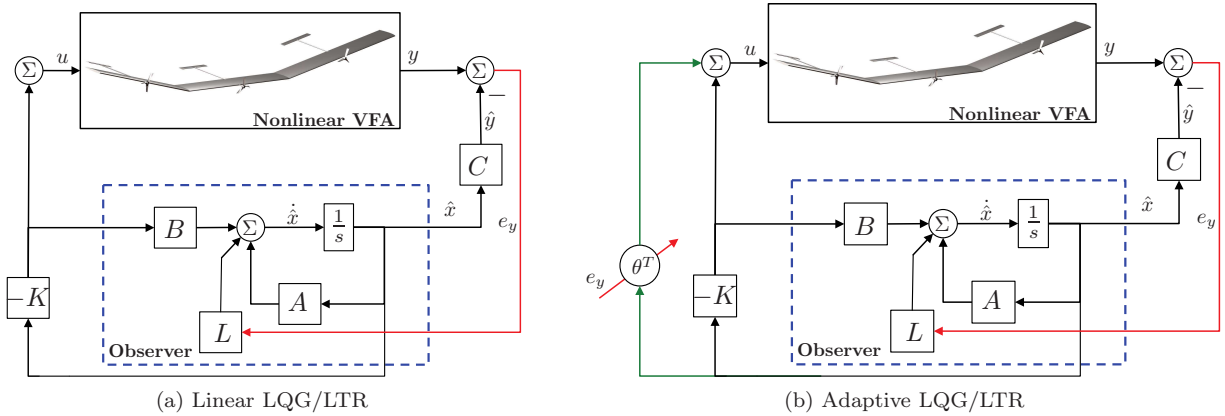

(a) Linear LQG/LTR   (b) Adaptive LQG/LTR

Figure 9: Comparison of adaptive and linear controller to dihedral disturbance.

American Institute of Aeronautics and Astronautics

IV.A. Comparison of linear and adaptive controllers

For the simulation studies that follows the aircraft was initially trimmed at an altitude of 40,000 ft, a speed of 30 ft/s with a dihedral angle of 5 deg. Then, similar to what was done in the open–loop study, the initial condition on the dihedral angle was changed to 25 deg and then the simulation was started. Also, to ensure that the controllers were not achieving good performance while sacrificing robustness to actuator dynamics, a first order actuator model with a pole at -20 rad/s was added to each control surface. A complete list of the free design parameters used to build the controllers can be found in Table 2.

A comparison of the linear and adaptive controllers over the first 40 seconds of the simulation study can be found in Figure 10. The adaptive controller dampens the oscillations in the dihedral angle and angle of attack more rapidly than the linear controller. This is at the cost of higher amplitude and slightly higher frequency oscillations in the inner elevator and outer ailerons, but still within the bandwidth of the actuator dynamics. The adaptive control inputs deviate from the linear control inputs from the beginning of the simulation, as both the elevator and the ailerons are increasing in value. Positive flap values lead to increased lift. This behavior is to be expected for a stabilizing controller as the increased dihedral reduces the total lift on the aircraft.

The results shown in Figure 10 illustrate the short period dynamics of the aircraft. For insight into the phugoid dynamics the same simulation results are compared for the velocity and dihedral angle of the VFA
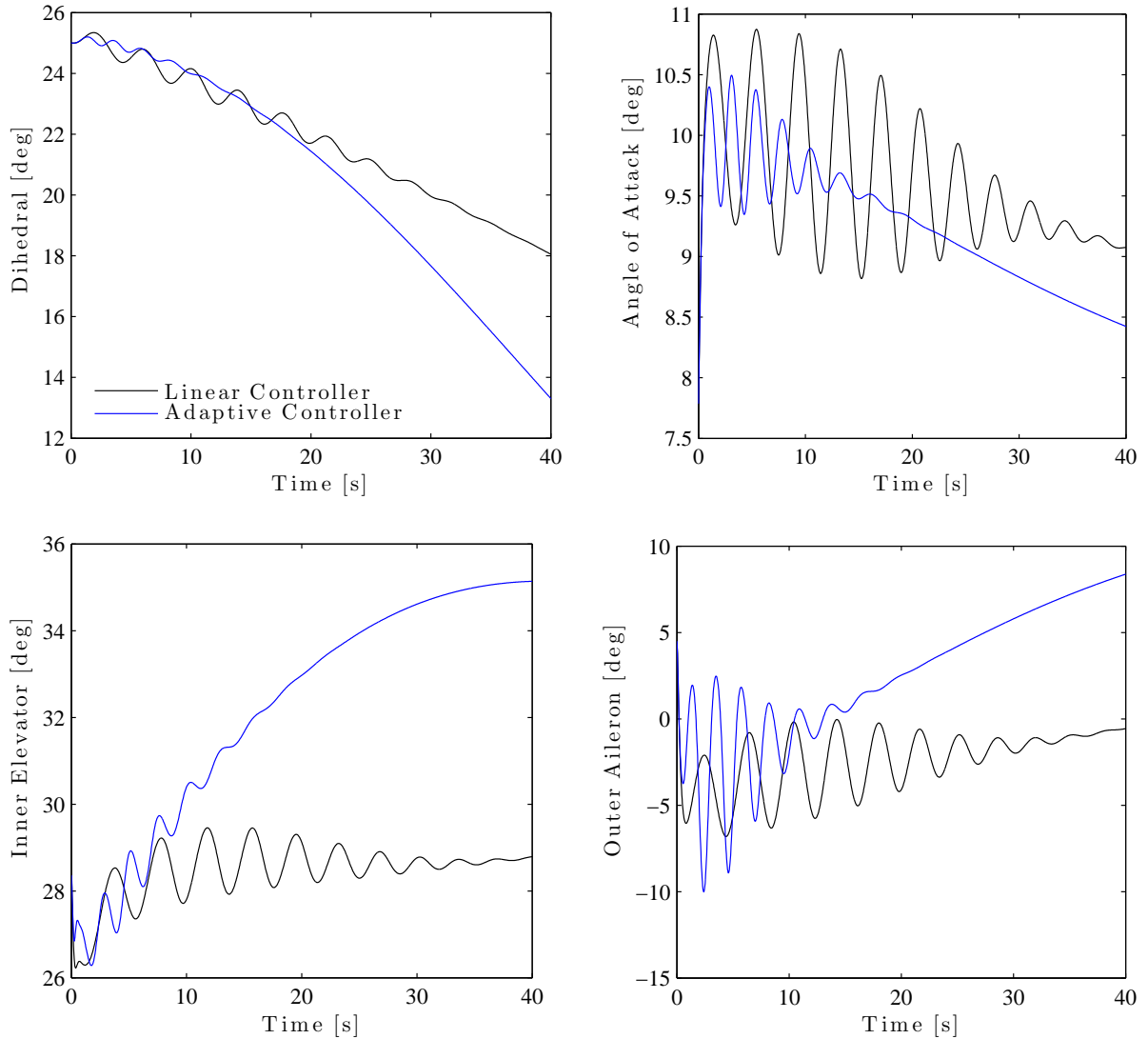

Figure 10: Comparison of adaptive and linear controller to dihedral disturbance.
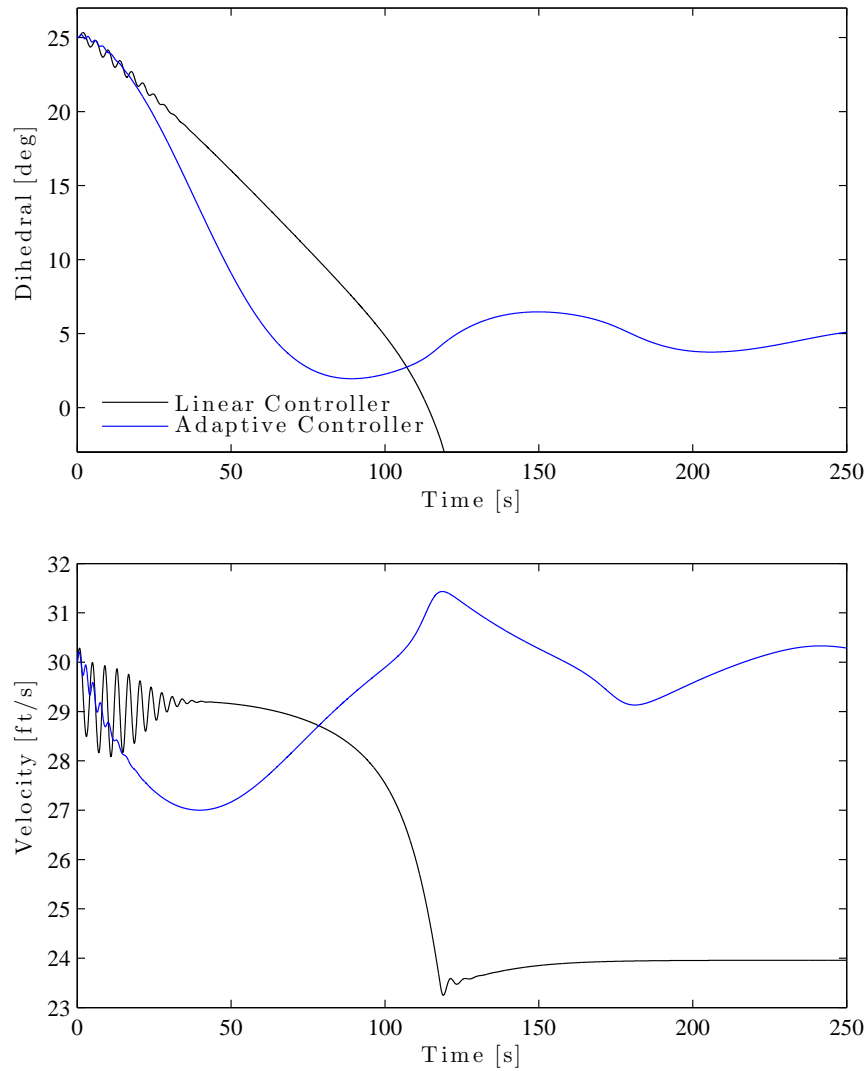
Figure 11: Expanded time to illustrate phugoid mode characteristics of simulation study.

over a 250 second window, see Figure 11. The adaptive controller returns the dihedral to trim more rapidly and in a stable fashion as compared to the linear controller. By observing the velocity trajectories the linear controller portrays an unstable phugoid divergence clearly seen after 50 seconds. For a purely linear system of equations with no linearization error the baseline linear controller is guaranteed to be stable for all initial conditions. However, given that the actual system is nonlinear, those stability characteristics of the baseline controller do not hold and the linear controller does not return the aircraft to trim. It appears that the baseline controller has achieved stability at a velocity of 24 ft/s per second. However, several control surfaces in the aircraft have exceeded 45 degrees and the large velocity divergence seen from 50 to 120 seconds is undesirable.

V.   Conclusions

A model sufficient for control design of VFA has been presented that captures instability in the phugoid mode. After comparing the linear LQG/LTR and adaptive LQG/LTR it was observed that the adaptive controller was better suited at stabilizing the aircraft during large dihedral excursions. This work however leaves much to be desired. Although the phugoid instability was captured by this model, the mechanism of generating large dihedral during flight was not illustrated. Two mechanisms, gusts and turbulence, have been proposed as disturbances that can generate large dihedral changes. Adding wind disturbances to this model

American Institute of Aeronautics and Astronautics

is underway. Second, the stability properties of adaptive LQG/LTR controllers for LTI matrices has been presented in.[21] However, the stability of the adaptive controller for LTV systems has not been rigorously proven. Work on that analysis is currently underway as well.

VI.   Acknowledgments

References

[1] Noll, T. E., Brown, J. M., Perez-Davis, M. E., Ishmael, S. D., Tiffany, G. C., and Gaier, M., "Investigation of the Helios Prototype Aircraft Mishap Volume I: Mishap Report," *NASA*, 2004.

[2] Langford, J., "The Daedalus Project: A Summary of Lessons Learned," *AIAA 89–2048*, 1989.

[3] Drela, M., "Aerodynamics of Human–Powered Flight," *Annu. Rev. Fluid Mech.*, Vol. 23, 1991.

[4] Allen, B., "Winged Victory of "Gossamer Albatross"," *National Geographic*, 1979.

[5] Zerweckh, S. H., von Flotow, A. H., and Murray, J. E., "Flight Testing a Highly Flexible Aircraft: Case Study on the MIT Light Eagle," *J. Aircraft*, 1990.

[6] van Schoor, M. C. and von Flotow, A. H., "Aeroelastic Characteristics of a Highly Flexible Aircraft," *J. Aircraft*, Vol. 20, No. 10, 1990.

[7] Drela, M., "Method for Simultaneous Wing Aerodynamic and Structural Load Prediction," *J. Aircraft*, 1990.

[8] Drela, M., "Integrated Simulation model for preliminary aerodynamic, structural, and control–law design of aircraft," *AIAA–99-1394*, 1999.

[9] Patil, M. J. and Hodges, D. H., "Flight Dynamics of Highly Flexible Flying Wings," *Journal of Aircraft*, Vol. 43, No. 6, 2006.

[10] Raghavan, B. and Patil, M., "Flight Dynamics of High Aspect–Ratio Flying Wings: Effect of Large Trim Deformation," *AIAA 2007–6386*, 2007.

[11] Su, W. and Cesnik, C. E. S., "Dynamic Response of Highly Flexible Flying Wings," *AIAA Journal*, Vol. 49, No. 2, 2011.

[12] Cesnik, C. E. S. and Su, W., "Nonlinear Aeroelastic Simulation of X–Hale: a Very Flexible UAV," *AIAA 2011–1226*, 2011.

[13] Cesnik, C. E. S., Senatore, P. J., Su, W., Atkins, E. M., Shearer, C. M., and Pitcher, N. A., "X–Hale: A Very Flexible UAV for Nonlinear Aeroelastic Tests," *AIAA 2010–2715*, 2010.

[14] Shearer, C. M. and Cesnik, C. E. S., "Nonlinear Flight Dynamics of Very Flexible Aircraft," *Journal of Aircraft*, Vol. 44, No. 5, 2007.

[15] Gregory, I. M., "Dynamic inversion to control large flexible transport aircraft," *AIAA–98–4323*, 1998.

[16] Gregory, I. M., "Modified Dynamic Inversion to Control Large Flexible Aircraft – What's Going On?" *AIAA 99–3998*, 1999.

[17] Gregory, I. M., "Stability Result for Dynamic Inversion Devised to Control Large Flexible Aircraft," *AIAA 2001–4284*, 2001.

[18] Gregory, I. M., *Design and stability analysis of an integrated controller for highly flexible advanced aircraft utilizing the novel nonlinear dynamic inversion*, Ph.D. thesis, California Institute of Technology, 2004.

[19] Shearer, C. M. and Cesnik, C. E. S., "Trajectory Control for Very Flexible Aircraft," *JGCD*, Vol. 31, No. 2, 2008.

[20] Raghavan, B. and Patil, M., "Flight Control for Flexible, High Aspect Ratio Flying Wings," *JGCD*, Vol. 33, No. 1, 2010.

[21] Lavretsky, E., "Adaptive Output Feedback Design Using Asymptotic Properties of LQG/LTR Controllers," *AIAA 2010–7538*, 2010.

[22] DeAngelis, V. M., "In–Flight Deflection Measurement of the HiMat Aeroelastically Tailored Wing," *J. Aircraft*, 1982.

A. Aircraft Properties

Table 1: Constants.

Variable	Value	Units
m^*	100	[slugs]
I_{xx}^*	200	[slugs ft^2]
I_{yy}^*	20	[slugs ft^2]
I_{zz}^*	160	[slugs ft^2]
s	80	[ft]
c_w	8	[ft]
c_t	2	[ft]
l_b	36	[ft]
S_w^*	640	[ft^2]
S_t^*	40	[ft^2]
$C_{\mathcal{L}_\alpha}$	2π	[-]
$C_{\mathcal{L}_\delta}$	2	[-]
$C_{\mathcal{M}_0}$	0.025	[-]
$C_{\mathcal{M}_\delta}$	-0.25	[-]
$C_{\mathcal{D}_0}$	0.007	[-]
$\kappa_\mathcal{D}$	0.07	[-]
κ_c	$1.4 \cdot 10^5$	[lbf/s]
κ_k	70^2	[lbf]

B. Detailed steps in Derivation of HSV Dynamics

B.1. Expansion of $\mathbf{H}_j^*$

From (28) the angular momentum can be expressed with respect to the velocity of point d through the following steps:

$$
\begin{aligned}
\mathbf{H}_j^* = {} & \left(-\tfrac{s}{2}m^* v_{c,z3} + I_{x_3 x_3}^* \dot{\eta}\right) \hat{\mathbf{x}}_3 \\
& + \left(I_{y_3 y_3}^* \cos(\eta)\omega_{d,y_2}\right) \hat{\mathbf{y}}_3 \\
& + \left(\tfrac{s}{2}m^* v_{c,x3} - I_{z_3 z_3}^* \sin(\eta)\omega_{d,y2}\right) \hat{\mathbf{z}}_3
\end{aligned}
\tag{64}
$$

$$
\mathbf{v}_d^{\{2\}} = \begin{bmatrix} v_{d,x_2} \\ 0 \\ v_{d,z_2} \end{bmatrix}
\tag{65}
$$

$$
\mathbf{v}_b^{\{2\}} = \mathbf{v}_j^{\{2\}} \begin{bmatrix} v_{d,x_2} + \tfrac{s}{3}\sin(\eta)\omega_{d,y_2} \\ 0 \\ v_{d,z_2} + \tfrac{s}{3}\cos(\eta)\dot{\eta} \end{bmatrix}
\tag{66}
$$

$$
\mathbf{v}_j^{\{3\}} = \begin{bmatrix} 1 & 0 & 0 \\ 0 & \cos\eta & \sin\eta \\ 0 & -\sin(\eta) & \cos(\eta) \end{bmatrix} \begin{bmatrix} v_{d,x_2} + \tfrac{s}{3}\sin(\eta)\omega_{d,y_2} \\ 0 \\ v_{d,z_2} + \tfrac{s}{3}\cos(\eta)\dot{\eta} \end{bmatrix} = \begin{bmatrix} v_{d,x_2} + \tfrac{s}{3}\sin(\eta)\omega_{d,y_2} \\ \left(v_{d,z_2} + \tfrac{s}{3}\cos(\eta)\dot{\eta}\right)\sin(\eta) \\ \left(v_{d,z_2} + \tfrac{s}{3}\cos(\eta)\dot{\eta}\right)\cos(\eta) \end{bmatrix}
\tag{67}
$$

$$
\mathbf{v}_c^{\{3\}} = \mathbf{v}_j^{\{3\}} + \boldsymbol{\omega}_3^{\{3\}} \times -\frac{s}{2}\hat{\mathbf{y}}_3
\tag{68}
$$

$$\mathbf{v}_c^{\{3\}} = \begin{bmatrix} v_{d,x_2} - \frac{s}{6}\sin(\eta)\omega_{d,y_2} \\ \left(v_{d,z_2} + \frac{s}{3}\cos(\eta)\dot{\eta}\right)\sin(\eta) \\ \left(v_{d,z_2} + \frac{s}{3}\cos(\eta)\dot{\eta}\right)\cos(\eta) - \dot{\eta}\frac{s}{2} \end{bmatrix} \tag{69}$$

B.2.   The time derivative of $\mathbf{H}_j^*$

Taking the time derivative of $\mathbf{h_1}$, $\mathbf{h_2}$, $\mathbf{h_3}$, successively

$$\frac{d}{dt}\mathbf{h_1} = \left(-\frac{s}{2}m^*\left(\dot{v}_{d,z_2}\cos(\eta) - v_{d,z_2}\sin(\eta)\dot{\eta} + \frac{s}{3}\cos^2(\eta)\ddot{\eta} - 2\frac{s}{3}\cos(\eta)\sin(\eta)\dot{\eta}^2\right) + \left(I^*_{x_3 x_3} + m^*\frac{s^2}{4}\right)\ddot{\eta}\right)\hat{\mathbf{x}}_3$$
$$+ \left(-\frac{s}{2}m^*\left(v_{d,z_2}\cos(\eta) + \frac{s}{3}\cos^2(\eta)\dot{\eta}\right) + \left(I^*_{x_3 x_3} + m^*\frac{s^2}{4}\right)\dot{\eta}\right)\frac{d}{dt}\hat{\mathbf{x}}_3 \tag{70}$$

and noting that $\frac{d}{dt}\hat{\mathbf{x}}_3 = (-\cos(\eta)\omega_{d,y_2}\hat{\mathbf{z}}_3 - \sin(\eta)\omega_{d,y_2}\hat{\mathbf{y}}_3)$, simplifies to

$$\frac{d}{dt}\mathbf{h_1} = \left(-\frac{s}{2}m^*\left(\dot{v}_{d,z_2}\cos(\eta) - v_{d,z_2}\sin(\eta)\dot{\eta} + \frac{s}{3}\cos^2(\eta)\ddot{\eta} - 2\frac{s}{3}\cos(\eta)\sin(\eta)\dot{\eta}^2\right) + \left(I^*_{x_3 x_3} + m^*\frac{s^2}{4}\right)\ddot{\eta}\right)\hat{\mathbf{x}}_3$$
$$+ \left(-\frac{s}{2}m^*\left(v_{d,z_2}\cos(\eta) + \frac{s}{3}\cos^2(\eta)\dot{\eta}\right) + \left(I^*_{x_3 x_3} + m^*\frac{s^2}{4}\right)\dot{\eta}\right)(-\cos(\eta)\omega_{d,y_2}\hat{\mathbf{z}}_3 - \sin(\eta)\omega_{d,y_2}\hat{\mathbf{y}}_3) \tag{71}$$

$$\frac{d}{dt}\mathbf{h_2}\left(I^*_{y_3 y_3}\cos(\eta)\dot{\omega}_{d,y_2} + I^*_{y_3 y_3}(-\sin(\eta)\dot{\eta}\omega_{d,y_2})\right)\hat{\mathbf{y}}_3 + \left(I^*_{y_3 y_3}\cos(\eta)\omega_{d,y_2}\right)(\dot{\eta}\hat{\mathbf{z}}_3 + \sin(\eta)\omega_{d,y_2}\hat{\mathbf{x}}_3) \tag{72}$$

$$\frac{d}{dt}\mathbf{h_3} = \left(\frac{s}{2}m^*\left(\dot{v}_{d,x_2} - \frac{s}{6}\cos(\eta)\dot{\eta}\omega_{d,y_2} - \frac{s}{6}\sin(\eta)\dot{\omega}_{d,y_2}\right) - I^*_{z_3 z_3}\left(\sin(\eta)\dot{\omega}_{d,y2} + \cos(\eta)\dot{\eta}\omega_{d,y_2}\right)\right)\hat{\mathbf{z}}_3$$
$$+ \left(\frac{s}{2}m^*\left(v_{d,x_2} - \frac{s}{6}\sin(\eta)\omega_{d,y_2}\right) - I^*_{z_3 z_3}\sin(\eta)\omega_{d,y2}\right)(\cos(\eta)\omega_{d,y_2}\hat{\mathbf{x}}_3 - \dot{\eta}\hat{\mathbf{y}}_3) \tag{73}$$

and collecting only the components in the x_3 axis only:

$$-\frac{s}{2}m^*\left(\dot{v}_{d,z_2}\cos(\eta) - v_{d,z_2}\sin(\eta)\dot{\eta} - s3\cos^2(\eta)\ddot{\eta} + 2\frac{s}{3}\cos(\eta)\sin(\eta)\dot{\eta}^2\right) + \left(I^*_{x_3 x_3} + m^*\frac{s^2}{4}\right)\ddot{\eta}$$
$$+ \left(I^*_{y_3 y_3}\cos(\eta)\omega_{d,y_2}\right)\sin(\eta)\omega_{d,y_2} \tag{74}$$
$$\left(\frac{s}{2}m^*\left(v_{d,x_2} - \frac{s}{6}\sin(\eta)\omega_{d,y_2}\right) - I^*_{z_3 z_3}\sin(\eta)\omega_{d,y2}\right)\cos(\eta)\omega_{d,y_2}.$$

B.3.   Local Velocity, Angles of Attack and Side Slip Angle

Local wind axis for frame–2

$$\alpha_2 = \arctan\left(\frac{V\sin\alpha + \dot{\eta}\frac{s}{3}\cos\eta}{V\sin\alpha + q\frac{s}{3}\sin\eta}\right) \tag{75}$$
$$\beta_2 = 0$$

$$V_2 = \sqrt{\left(V\cos\alpha + q\frac{s}{3}\sin\eta\right)^2 + \left(V\sin\alpha + \dot{\eta}\frac{s}{3}\cos\eta\right)^2} \tag{76}$$

Local wind axis for frames 1 and 3

$$\alpha_3 = \alpha_1 = \arctan\left(\frac{\left(V\sin\alpha + \dot{\eta}\frac{s}{3}\cos\eta\right)\cos\eta - \dot{\eta}\frac{s}{2}}{V\sin\alpha - q\frac{s}{6}\sin\eta}\right)$$
$$\beta_3 = -\beta_1 = \arcsin\left(\frac{\left(V\sin\alpha + \dot{\eta}\frac{s}{3}\cos\eta\right)\sin\eta}{V_3}\right) \tag{77}$$

$$V_3 = \sqrt{\left(V\sin\alpha - q\frac{s}{6}\sin\eta\right)^2 + \left(\left(V\sin\alpha + \dot{\eta}\frac{s}{3}\cos\eta\right)\sin\eta\right)^2 + \left(\left(V\sin\alpha + \dot{\eta}\frac{s}{3}\cos\eta\right)\cos\eta - \dot{\eta}\frac{s}{2}\right)^2} \tag{78}$$

and $V_1 = V_3$

American Institute of Aeronautics and Astronautics

C.   Projection Operator

The convex function parameter is defined as

$$F(\theta; \vartheta, \varepsilon) = [f_1(\theta_1) \ \ldots \ f_m(\theta_m)]^T \tag{79}$$

, $\theta = [\theta_1 \ \ldots \ \theta_m] \in \mathbb{R}^{n \times m}$, each f_i is a convex function of the form

$$f_i(\theta_i) = \frac{\|\theta_i\|^2 - \vartheta^2}{2\varepsilon\vartheta + \varepsilon^2}. \tag{80}$$

Definition 1 (Projection Operator).

$$\text{Proj}(\theta, y, F(\theta; \vartheta, \varepsilon)) = [\text{proj}(\theta_1, y_1, f_1(\theta_1)) \ \ldots \ \text{proj}(\theta_m, y_m, f_m(\theta_m))] \tag{81}$$

where $y = [y_1 \ \ldots \ y_m] \in \mathbb{R}^{n \times m}$ and

$$\text{proj}(\theta_j, y_j, f_j(\theta_j)) = \begin{cases} y_j - \frac{\nabla f_j(\theta_j)(\nabla f_j(\theta_j))^T}{\|\nabla f_j(\theta_j)\|^2} y_j f_j(\theta_j) & \text{if } f_j(\theta_j) > 0 \wedge y_j^T \nabla f_j(\theta_j) > 0 \\ y_j & \text{otherwise} \end{cases} \tag{82}$$

$j = 1$ to m.

D.   Control Design Parameters

Table 2: Control Design Parameters.

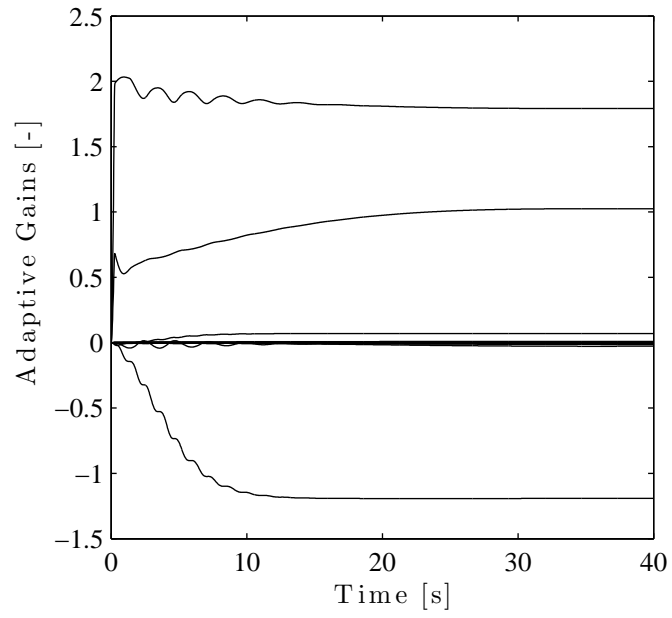| Variable	Value
Q_0	$I^{7 \times 7}$
R_0	200
λ	0.001
ν	0.3
Q_c	$\text{diag}\big([1 \ 10 \ 0.01 \ 10 \ 1 \ 1 \ 100]^T\big)$
R_c	$\text{diag}\big([10 \ 10 \ 30]^T\big)$;
Γ	$10 \cdot \text{diag}\big([0.1 \ 300 \ 0.0001 \ 1 \ 1 \ 1 \ 0.00001]^T\big)$
ϑ	2
ε	0.2

E. Plots

Figure 12: Adaptive Gains.